Energy & Environmental Science

ROYAL SOCIETY OF CHEMISTRY

PAPER

View Article Online
View Journal | View Issue





Cite this: *Energy Environ. Sci.*, 2024, **17**, 7944

# Stabilizing $LiCoO_2$ at 4.6 V by regulating anti-oxidative solvents†

Hengyu Ren,‡[a] Guorui Zheng,‡*[ab] Yuhang Li,[b] Shiming Chen,[a] Xiaohu Wang,[a] Mingzheng Zhang,[a] Wenguang Zhao,[a] Haocong Yi,[a] Weiyuan Huang,[c] Jianjun Fang,[ad] Tongchao Liu,[c] Luyi Yang,[a] Ming Liu,*[b] Qinghe Zhao*[a] and Feng Pan*[a]

For $LiCoO_2$ (LCO) operating at high voltages (>4.5 V *vs.* $Li/Li^+$), the intensive side reactions between LCO and traditional ethylene carbonate (EC)-based electrolytes with $LiPF_6$ salts can produce plenty of corrosive species (such as HF and $HPO_2F_2$), causing severe surface degradation. Herein, anti-oxidative fluoroethylene carbonate (FEC) and difluoroethylene carbonate (DFEC) were selected as co-solvents to reduce the generation of corrosive species. Besides, $PF_6^-$ anions enrich the Helmholtz plane of the LCO/electrolyte interface and promote the formation of a robust cathode/electrolyte interphase (CEI) featuring $LiF/Li_xPO_yF_z/Li_3PO_4$ inorganics and P-containing organics under the synergy of fluorinated solvents, which significantly inhibits the catalysis of highly oxidative $Co^{4+}/O^{n-}$ ($0 < n < 2$). Benefiting from the reduced corrosive species and reinforced CEI, the layered structure of the LCO surface is well preserved during long-term cycling, with a highly reversible O3/H1-3 phase transition. Consequently, a LCO||graphite pouch cell exhibits a remarkable capacity retention of 85.7% after 500 cycles in 3.0–4.55 V. This work provides a new insight into developing advanced functional electrolytes for high-voltage lithium-ion batteries.

Received 11th May 2024,
Accepted 3rd September 2024

DOI: 10.1039/d4ee02049a

rsc.li/ees

## Broader context

In recent years, the growing demands for advanced high-energy-density lithium batteries have stimulated tremendous research interest for developing high-voltage $LiCoO_2$ (LCO) cathodes. However, the incompatibility of traditional commercial electrolytes against the highly delithiated LCO surface with strongly oxidative $Co^{4+}/O^{n-}$ ($0 < n < 2$) severely hinders their large-scale applications, mainly due to the excessive oxidation of solvents, especially in ethylene carbonate (EC)-based electrolytes, which can form acid-corrosive species (including HF and $HPO_2F_2$). In this study, by replacing EC with more anti-oxidative fluoroethylene carbonate (FEC) and difluoroethylene carbonate (DFEC) co-solvents, the enhanced structural stability of LCO at 4.6 V (*vs.* $Li/Li^+$) was achieved and the optimization mechanism was revealed. During cycling, due to the anti-oxidative characteristic of FEC/DFEC solvents, the layered structure of LCO was well maintained by reducing interface corrosive species, and the robust cathode/electrolyte interphase (CEI) enriched with LiF/P–O species was progressively constructed on the surface of LCO, ensuring the stability of the surface/interface region and reversibility of $Li^+$ (de)intercalation of LCO during long-term cycling.

## Introduction

$LiCoO_2$ (LCO) has long been the indispensable cathode material in the consumer electronics field, mainly due to its high volumetric energy density and high rate/cycling performances. With the acceleration of the lightweight tendency of new electronic products, the application of LCO cathodes calls for a higher cut-off voltage beyond 4.5 V (*vs.* $Li/Li^+$, hereafter) to release more reversible specific capacity with significantly enhanced energy density. However, high-voltage (HV) operation can seriously affect the stability of the LCO/electrolyte interface, which is mainly reflected in the severe interface parasitic

[a] *School of Advanced Materials, Peking University Shenzhen Graduate School, Peking University, Shenzhen 518055, P. R. China.*
*E-mail: zhengguorui1991@163.com, zhaoqh@pku.edu.cn, panfeng@pkusz.edu.cn*
[b] *Institute of Materials Research, Tsinghua Shenzhen International Graduate School, Tsinghua University, Shenzhen 518055, P. R. China.*
*E-mail: liuming@sz.tsinghua.edu.cn*
[c] *Chemical Sciences and Engineering Division, Argonne National Laboratory, Lemont, IL 60439, USA*
[d] *Qiantu battery Technology Co., Ltd, Dongguan 523808, P. R. China*

† Electronic supplementary information (ESI) available. See DOI: https://doi.org/10.1039/d4ee02049a

‡ H. R. and G. Z. contributed equally to this work.

reactions originating from the high catalytic oxidation activity of $Co^{4+}/O^{n-}$ ($0 < n < 2$) on the LCO surface, the surface structure degradation originating from Co/O loss, *etc.*[1–4] These issues further cause deteriorated $Li^+$ diffusion kinetics across the LCO surface and destroy the reversibility of bulk phase transitions, leading to crack formation and, consequently, rapid capacity decay.[5–8] To alleviate these issues, the optimization of interface properties, especially through electrolyte tuning, is the most efficient and low-cost route to stabilize the structure of LCO at high voltages.

As is known, commercially used electrolytes are usually composed of cyclic carbonate (such as ethylene carbonate (EC)) and linear carbonate (such as ethyl methyl carbonate (EMC) or diethyl carbonate (DEC)) solvents as well as low-concentration $LiPF_6$ salts. However, in most occasions, their combinations encounter difficulty in tolerating an HV operation beyond 4.5 V, showing severe electrochemical decomposition at both the LCO cathode and graphite/Li anode interfaces, as depicted in Fig. S1 (ESI†).[9] The continuous oxidation/dehydrogenation of EC/EMC solvents generate detrimental $H^+/H_2O$, accompanied with $CO/CO_2$ gas release.[2,10,11] Meanwhile, the increased $H^+/H_2O$ concentration further intensifies the decomposition (hydrolysis) of the $LiPF_6$ salt, forming plenty of corrosive species, such as HF, $HPO_2F_2$, $H_2PO_3F$, and $H_3PO_4$.[9,12] These corrosive species cause severe Co dissolution from the LCO surface, finally leading to its structure degradation and the formation of a fragile cathode/electrolyte interphase (CEI). It is noted that the Co dissolution from the LCO side has a cross effect on the Li metal or graphite anodes, *i.e.*, $Co^{2+}$ can deposit on the anode sides and further cause the passivation of anodes.[13] Therefore, enhancing the overall stability of the electrolyte to remove HF and $H_2O$ and forming a protective CEI to reduce undesirable interfacial reactions are the key breakthroughs to stabilize the LCO structure from the aspect of electrolyte tuning.

Compared to the traditional EC solvent, the emerging fluorinated cyclic carbonates (including fluoroethylene carbonate (FEC) and difluoroethylene carbonate (DFEC)) gradually show their great potential in HV applications due to the enhanced anti-oxidative properties.[14–19] Recently, they have been widely investigated as electrolyte additives or solvents in electrolytes, which can regulate the $Li^+$ solvation structure and promote the formation of a robust solid electrolyte interphase (SEI) on Li metal or Si/Si–C anodes.[16,20,21] As reported previously, with the increase in fluorination extents of solvents from EC, FEC to DFEC, the $Li^+$ desolvation energy from the electrolytes decreases with the promoted $Li^+$ transport kinetics, finally contributing to the improved low-temperature performance.[18] In addition, the FEC and DFEC are promising reducible sacrificial agents to help reconstruct the robust SEI on the anode with a certain amount of LiF, $ROCO_2Li$ and polymeric species, especially utilizing their synergetic effects.[20,22,23] Despite these insights, the detailed optimization mechanism of FEC/DFEC solvents on enhancing the HV cycle performance of LCO still remains vague and requires further investigation.

In this work, the optimization mechanism by the rational control of electrolyte solvents from EC to FEC/DFEC solvents was systematically explored based on comprehensive characterizations and theoretical simulations. We found that the enhanced stability of LCO in an anti-oxidative FEC–DFEC-based electrolyte is basically attributed to reduced corrosive species and the formation of robust and uniform CEI, which significantly reduce the catalysis of highly oxidative $Co^{4+}/O^{n-}$ ($0 < n < 2$) and play important roles in stabilizing the surface structure as well as enhancing the phase transition reversibility of LCO. Specifically, under the synergy of anti-oxidative and weak-solvated fluorinated solvents, the reaction path of $PF_6^-$ anions in the inner Helmholtz plane of the LCO/electrolyte interface is regulated, which reduces the hydrolysis of $PF_6^-$ to form corrosive species such as HF and $HPO_2F_2$, but to promote the formation of robust CEI abundant with $LiF/Li_xPO_yF_z/Li_3PO_4$ inorganics and P-containing organics. As a result, the LCO cathode shows significantly enhanced rate capability and long-term cycling stability with a high capacity retention of 85.5% after 1000 cycles in LCO||Li cells between 3.0–4.6 V and 85.7% after 500 cycles in LCO||graphite pouch cells between 3.0–4.55 V.

## Results and discussion

### Electrolyte regulation

Starting with the most basic electrolyte system comprising commonly used solvents of cyclic and linear carbonates (EC/EMC), given that the DEC is more stable than EMC, and the fluorinated EC solvents (FEC/DFEC) have enhanced anti-oxidation properties, five types of electrolytes are rationally designed to understand the effects of solvent tuning on the electrochemical stability upon HV operation, as listed in Table S1 (ESI†). As illustrated in linear sweep voltammetry (LSV) results (Fig. S2, ESI†), the partial replacement of EMC by DEC can inhibit the drastic oxidative decomposition of electrolytes to a certain extent. Besides, further replacing EC with fluorinated solvents (FEC/DFEC) exhibits an extended electrochemical window to higher potentials. Therefore, it is necessary to understand the effects of solvent's tuning on its physicochemical properties and resulting cell performances. As reported previously, there always exists an electrical double layer (EDL) between the electrode surface and the electrolyte, called the Helmholtz plane, which includes the inner Helmholtz plane (IHP) and outer Helmholtz plane (OHP). Generally, the OHP contains $Li^+$ ions inside the solvation shells, and the IHP contains anions and organic molecules adsorbed on the LCO/electrolyte interface.[2,24,25] Specifically, the difference in the solvation structures of OHP will significantly affect the (de)solvation kinetics of $Li^+$ ions and the chemical species in IHP, finally leading to a distinct CEI layer.

We first analyzed the interaction between the $Li^+$ ions and the solvents (including EC, FEC, and DFEC) *via* density functional theory (DFT) calculations. The calculated binding affinity can qualitatively evaluate the interaction strength between the

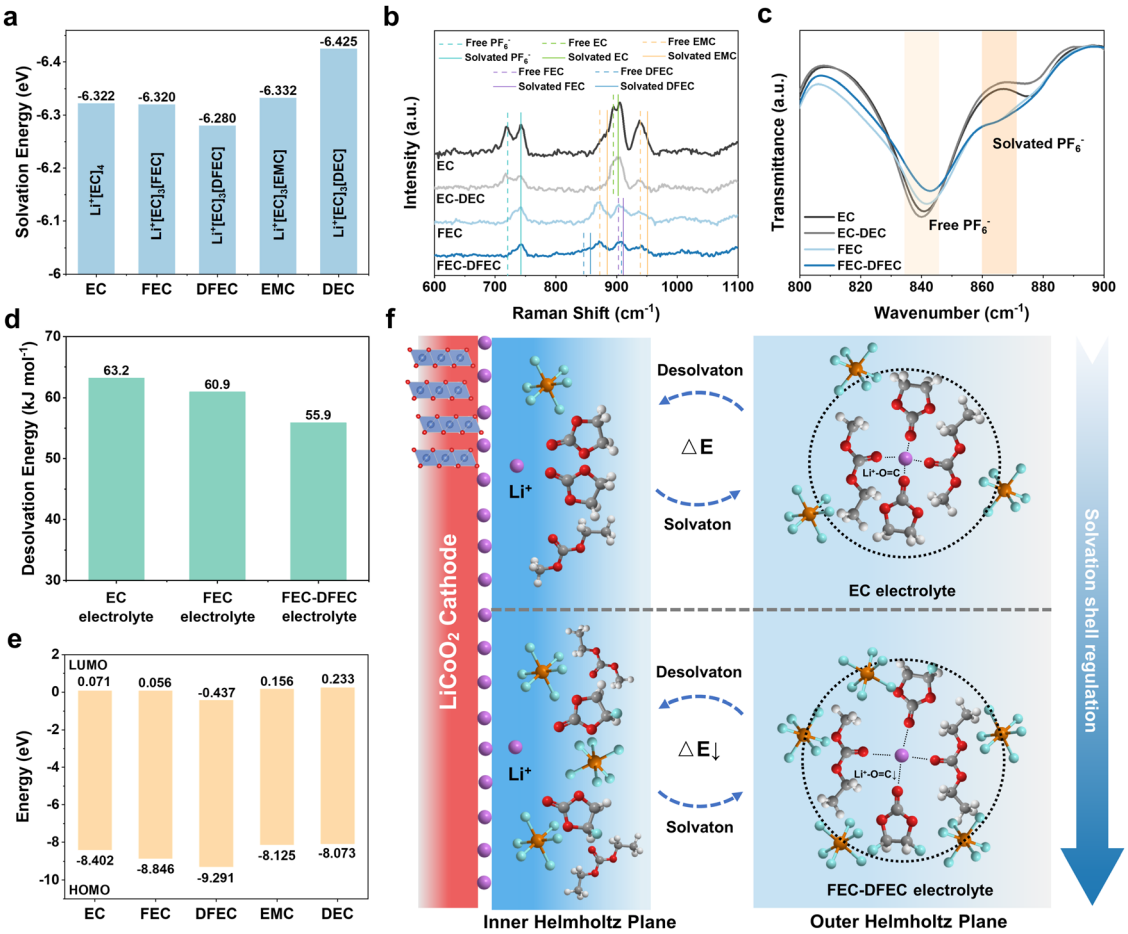


Fig. 1 Influence of electrolyte regulation on the Helmholtz plane. (a) Calculated $Li^+$ solvation energy in the $Li^+[solvents]_4$ solvation structure. (b) Raman spectra and (c) FTIR spectra of EC, EC–DEC, FEC and FEC–DFEC electrolytes. (d) $Li^+$ desolvation energy in EC, FEC and FEC–DFEC electrolytes by fitting the $R_{ct}$ of $Li_{0.7}CoO_2||Li_{0.7}CoO_2$ symmetric cells obtained at different temperatures with the Arrhenius equation. (e) Calculated HOMO/LUMO energy of different solvents. (f) Schematic of the inner and outer Helmholtz plane regulation in the FEC–DFEC electrolyte.

$Li^+$ ions and the solvents.[18] As shown in Fig. S3a (ESI†), the binding affinity values of $Li^+$-fluorinated solvents are higher than that of $Li^+$–EC, indicating the weaker solvation strength between $Li^+$ ions and FEC/DFEC solvents. Fig. 1(a) and Fig. S3b (ESI†) further show the calculated $Li^+$ solvation energies in a $Li^+[solvents]_4$ solvation structure, and it is clear that the DFEC-derived one is the most prone to release free $Li^+$ ions, whether we replace one solvent molecule ($Li^+[EC]_3[DFEC]$) or replace all of them ($Li^+[DFEC]_4$). Besides, the necessary involvement of FEC solvents helps to stabilize the $Li^+$ solvation structure and to regulate the electrolytic viscosity to some extent.[26]

The difference in the $Li^+$–solvent interaction will greatly affect the coordination of the $PF_6^-$ anions in the solvation structure. In the Raman spectra of electrolytes (Fig. 1(b)), the peaks of Raman shift at about 720 and 740 $cm^{-1}$ correspond to the free and solvated $PF_6^-$, respectively. It can be seen that, the weaker the $Li^+$–solvent interaction, the higher the intensity of solvated $PF_6^-$. In Fig. 1(c) and Fig. S4a (ESI†), the results of Fourier transform infrared (FTIR) spectroscopy also indicate that less free $PF_6^-$ (840 $cm^{-1}$) and more solvated $PF_6^-$ (870 $cm^{-1}$) exist in the fluorinated electrolyte. Besides, in Fig. S4b (ESI†), the up-field shifts of $^7Li$ nuclear magnetic resonance (NMR) spectra in fluorinated electrolytes, which are EC-free and weakly solvated, further demonstrate the intensive $PF_6^-$-shielding effect on the $Li^+$ ions, corresponding well to the Raman and FTIR results.[27]

The temperature-dependent electrochemical impedance spectroscopy (EIS) measurements (Fig. S5, ESI†) were further applied to quantify the $Li^+$ desolvation kinetics on the LCO surface in different electrolytes.[28] We conducted the $Li_{0.7}CoO_2||Li_{0.7}CoO_2$ symmetric cell to exclude the effect of the CEI layer and prevent damage to the surface layer structure. The fitted results (Fig. 1(d) and Fig. S5, ESI†) show that the $Li^+$ desolvation energy in the FEC (60.9 kJ $mol^{-1}$) and FEC–DFEC (55.9 kJ $mol^{-1}$) electrolytes are obviously lower than that in the EC electrolyte (63.2 kJ $mol^{-1}$), exhibiting the facilitated $Li^+$ (de)solvation kinetics in FEC and FEC–DFEC electrolytes. In addition, the slight increase in the $Li^+$ desolvation energy in the DFEC electrolyte (61.6 kJ $mol^{-1}$) can be attributed to the synthetical effects of $Li^+$–solvents/anions, *i.e.*, the weak $Li^+$–DFEC interaction lead to the significantly enhanced $Li^+$–$PF_6^-$ interaction, resulting in the increased $Li^+$ desolvation energy.

 

During the cycle, the de-solvated $PF_6^-$ anions and solvents can gather in IHP to anticipate the interfacial reactions. The lowest unoccupied molecular orbital (LUMO) and highest occupied molecular orbital (HOMO) energies of the solvents were further calculated *via* DFT calculations, to reveal the potentials of the reduction/oxidation stability of organic solvents in IHP/OHP. Both the HOMO and LUMO energies of DFEC and FEC are lower than those of EC (Fig. 1(e)), which indicate their enhanced anti-oxidative stability on LCO side and preferential reduction to form the initial SEI on Li or graphite side. Furthermore, the HOMO and LUMO energies of different $Li^+[solvents]_4$ solvation structures (Fig. S6, ESI†) also indicate that completely replacing the EC solvent with FEC/DFEC solvents can dramatically enhance the anti-oxidative stability and reduction activity of the solvation structure.

As summarized in Fig. 1(f), the introduction of FEC/DFEC solvents can effectively regulate the IHP and OHP, causing weaker interactions between $Li^+$ ions and solvents, and more $PF_6^-$ anions participate in the $Li^+$ solvation sheath. On the one hand, in OHP, the lower $Li^+$ (de)solvation energy ensures the fast $Li^+$ transport kinetics. On the other hand, in IHP, more electrochemically anti-oxidative organic solvents and the $PF_6^-$ anion-dominant interface chemistry significantly promote the formation of chemo-mechanically stable CEI abundant with inorganic species during the cycle, thereby improving the compatibility of the regulated electrolyte with LCO at 4.6 V.

## Cell performances

The cell performances of the progressively optimized electrolytes were evaluated by assembling the LCO||Li cells. The correlated X-ray diffraction (XRD) results of pristine LCO are presented in Fig. S7 (ESI†), showing a pure layered α-$NaFeO_2$ structure with a space group of *R*-$\bar{3}m$. Transmission electron microscopy (TEM) characterizations and correlated diffraction patterns were further utilized to analyze the surface and bulk structures of LCO (Fig. S8, ESI†), both showing the characteristics of layered structures. The initial charge/discharge curves of LCO||Li cells (Fig. 2(a) and Fig. S9, ESI†) indicate that,

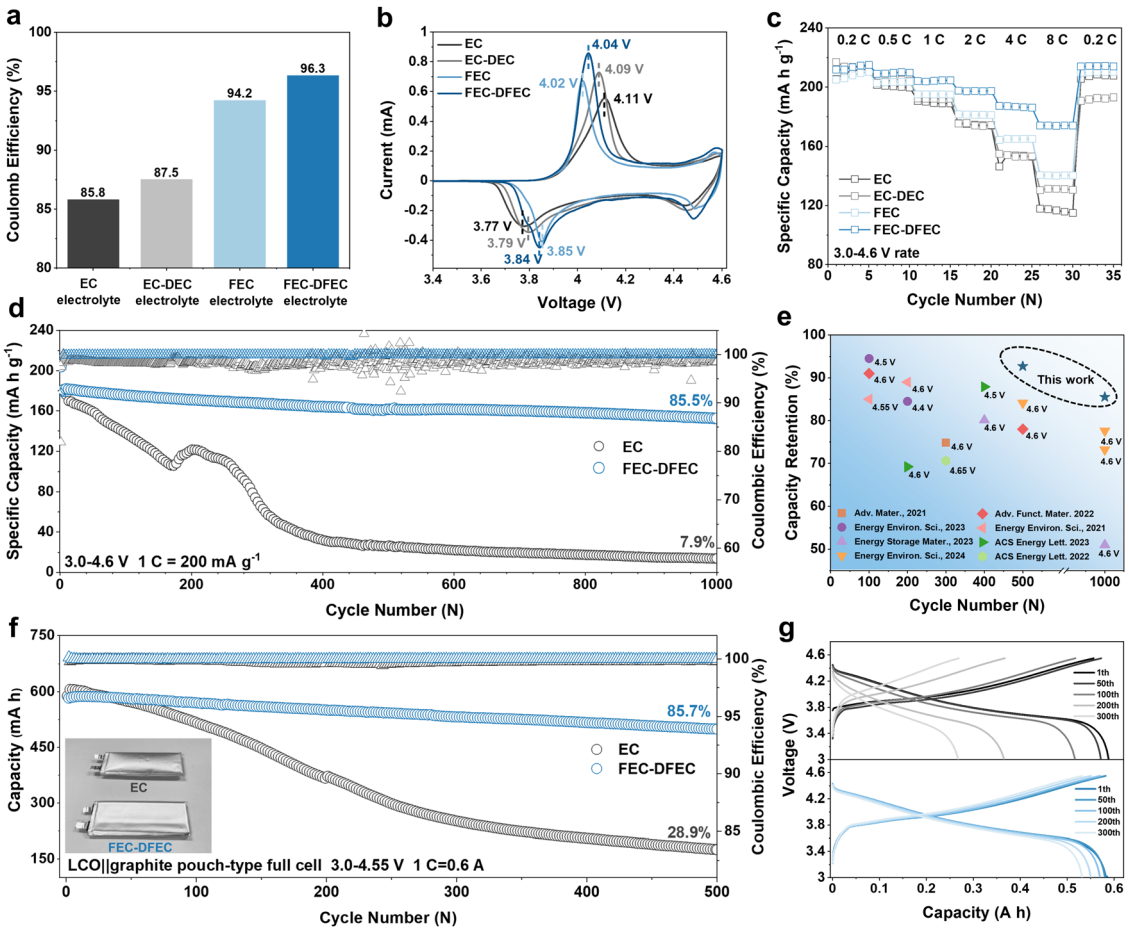


Fig. 2 Cell performances of LCO||Li cells and LCO||graphite pouch cells in different electrolytes. (a) ICE, (b) CV tests and (c) rate performances of LCO||Li half cells in the EC, EC–DEC, FEC, FEC–DFEC electrolytes in the voltage range of 3.0–4.6 V. (d) Cycling performance of LCO||Li half cells in EC and FEC–DFEC electrolytes in the voltage range of 3.0–4.6 V, at a current of 2C. (e) Comparison of cell performances of recently reported electrolyte regulation for LCO cathodes at room temperature. (f) Cycling performance of the LCO||graphite pouch type full cell in the voltage range of 3.0–4.55 V at 1C in the EC and FEC–DFEC electrolytes and the digital photograph of the pouch-type full cell after 500 cycles. (g) Corresponding charge and discharge curves at different cycles for the LCO||graphite pouch cell.

through regulating the solvents, it exhibits a high reversible discharge capacity of ~220 mA h $g^{-1}$ and a high initial Coulombic efficiency (ICE) of up to ~96.3% cycling in the FEC–DFEC electrolyte, while in the EC electrolyte, it exhibits a lower discharge capacity of ~218 mA h $g^{-1}$ and an ICE of lower than 90%, which are attributed to the reduced interface polarization and optimized interfacial reaction. The reduced interface polarization can be further confirmed by the cyclic voltammetry (CV) tests, as shown in Fig. 2(b) and Fig. S10 (ESI†). The LCO||Li cells cycled in FEC and FEC–DFEC electrolytes show a much smaller half-peak width and voltage hysteresis than that in the EC electrolyte, demonstrating the faster $Li^+$ transport kinetics.[29] Meanwhile, the lowest leakage current for LCO||Li cells is observed in FEC–DFEC electrolytes, which also indicate the optimized LCO/electrolyte interface with less detrimental side reactions (Fig. S11, ESI†). Hence, they display significantly improved rate capability and cycling stability, as shown in Fig. 2(c) and Fig. S12 (ESI†). At a high current density of 8C (1C = 200 mA $g^{-1}$), the discharge capacities of LCO||Li cells cycled in EC, EC–DEC, FEC and FEC–DFEC electrolytes are 116.6, 131.2, 140.1, and 173.9 mA h $g^{-1}$, respectively. Meanwhile, after 500 cycles at a rate current of 1C, the capacity retention of LCO||Li cells in the EC, EC–DEC, FEC and FEC–DFEC electrolytes are 37.7%, 61.4%, 83.2% and 92.7%, respectively. Impressively, the LCO||Li cell using an FEC–DFEC electrolyte shows a high capacity retention of 85.5% after 1000 cycles at 2C (Fig. 2(d)), which is among the best reported cycling performances (Fig. 2(e) and Table S2, ESI†). Besides, the comparison of long-term cyclic charge/discharge curves of LCO||Li cells in different electrolytes (Fig. S13 and S14, ESI†) and the evolution of correlated charge/discharge average voltages upon cycles (Fig. S15, ESI†) were performed, and the results indicated the detrimental structural degradation occurring on LCO with severe voltage decay in the EC electrolyte. While in the FEC–DFEC electrolyte, the charge/discharge curves almost overlap with nearly no change in charge/discharge average voltages within 200 cycles, further confirming the beneficial effects of the solvent regulation. Theoretically, due to the anti-oxidative property of DFEC, the cells in the DFEC electrolyte can achieve much better cell performances than those in the FEC–DFEC electrolyte. However, as shown in Fig. S16 (ESI†), although the LCO||Li cell using the DFEC electrolyte also shows a high capacity retention of 89.6% after 500 cycles at 1C with significantly reduced voltage decay, the incompatibility between DFEC electrolyte and Li anode leads to some negative results, including low Coulombic efficiency during cycling and the poor stability of Li||Li symmetric cells, which is attributed to the massive consumption of DFEC on the Li anode.[20] In contrast, the FEC–DFEC electrolyte shows better compatibility with the Li anode, and the correlated Li||Li symmetric cell shows superior plating/striping cycling stability with low over-potential for over 500 h (Fig. S17, ESI†). For comparison, the Li||Li symmetric cell with the EC electrolyte shows evident fluctuation in voltage hysteresis and suffers from a sudden short-circuit at about 220 h.

The LCO||graphite pouch-type cells (with capacity of about 0.6 A h) were further fabricated to evaluate the feasibility of the designed FEC–DFEC electrolyte. As presented in Fig. 2(f) and (g), the LCO||graphite cell with the FEC–DFEC electrolyte presents an excellent cycling stability with a high capacity retention of 85.7% after 500 cycles in the voltage range of 3.0–4.55 V at 1C without visible swelling detected. When compared, the LCO||graphite full cell with the EC electrolyte shows a rapid capacity decay with obvious swelling upon cycles, indicating the severe electrolyte decomposition and interfacial side reactions. Besides, benefiting from the promoted $Li^+$ transport kinetics of the FEC–DFEC electrolyte, the LCO||graphite cell shows outstanding low-temperature performance with a high capacity retention of 88.2% at −20 °C compared with that at 25 °C (Fig. S18, ESI†).

### Reduced interfacial side reactions

The optimized LCO/electrolyte interfacial reaction is the origin of realizing its better electrochemical performances at 4.6 V. Herein, several *in situ* characterizations are combined to explore the optimization mechanism behind. In Fig. 3(a), the *in situ* Raman spectra of LCO||Li cells with EC and FEC–DFEC electrolytes are obtained for the initial two cycles in the voltage range of 3.0–4.6 V, and the correlated CV curves are shown in Fig. S19 (ESI†). The characteristic Raman peaks of LCO, located at the Raman shifts of 485 and 595 $cm^{-1}$, can be assigned to the O–Co–O bending mode ($E_g$) and Co–O stretching mode ($A_{1g}$), respectively.[30,31] It is noted that, for the EC electrolyte, when the voltage is beyond 4.2 V, the $E_g$ and $A_{1g}$ peaks disappear in the 1st cycle, and their intensity decreases significantly in the 2nd cycle, mainly attributed to the breakage of Co–O bonds, which is induced by the severe interfacial side reactions between highly oxidative $Co^{4+}/O^{n-}$ ($0 < n < 2$) and the EC electrolyte. This finally results in the structure degradation from "layered to spinel/rocksalt" on the LCO surface, since there appears a new peak at 670 $cm^{-1}$ in the Raman spectra after the cycles (Fig. S20, ESI†).[30,32] In contrast, in the FEC–DFEC electrolyte, the $E_g$ and $A_{1g}$ peaks remain constant during the cycle even charging to a high voltage of 4.6 V, indicating the stabilized Co–O bonds on the LCO surface. Besides, there is no signal observed at 670 $cm^{-1}$ after the cycles, illustrating the stabilized layered phase on the LCO surface.

Then, the *in situ* ultraviolet-visible spectrophotometry (UV-vis) was adopted to understand the chemical degradation of LCO.[33] As observed in Fig. 3(b), there are obvious signals of $Co^{2+}$ dissolution near the wavelength of ~500 nm upon charging LCO to 4.6 V in the EC electrolyte, which cannot be detected for the LCO cycled in the FEC–DFEC electrolyte and can be confirmed by the inductively coupled plasma-optical emission spectroscopy (ICP-OES) tests (Fig. S21, ESI†).[34] Since the low-valence Co ion's dissolution from the LCO surface is regarded as the result of HF corrosion and oxygen loss, it is reasonable to hypothesize that the modified solvation chemistry in the FEC–DFEC electrolyte is capable of constructing a protective CEI with the inhibited generation of corrosive HF species and reduced interfacial side reactions.

 

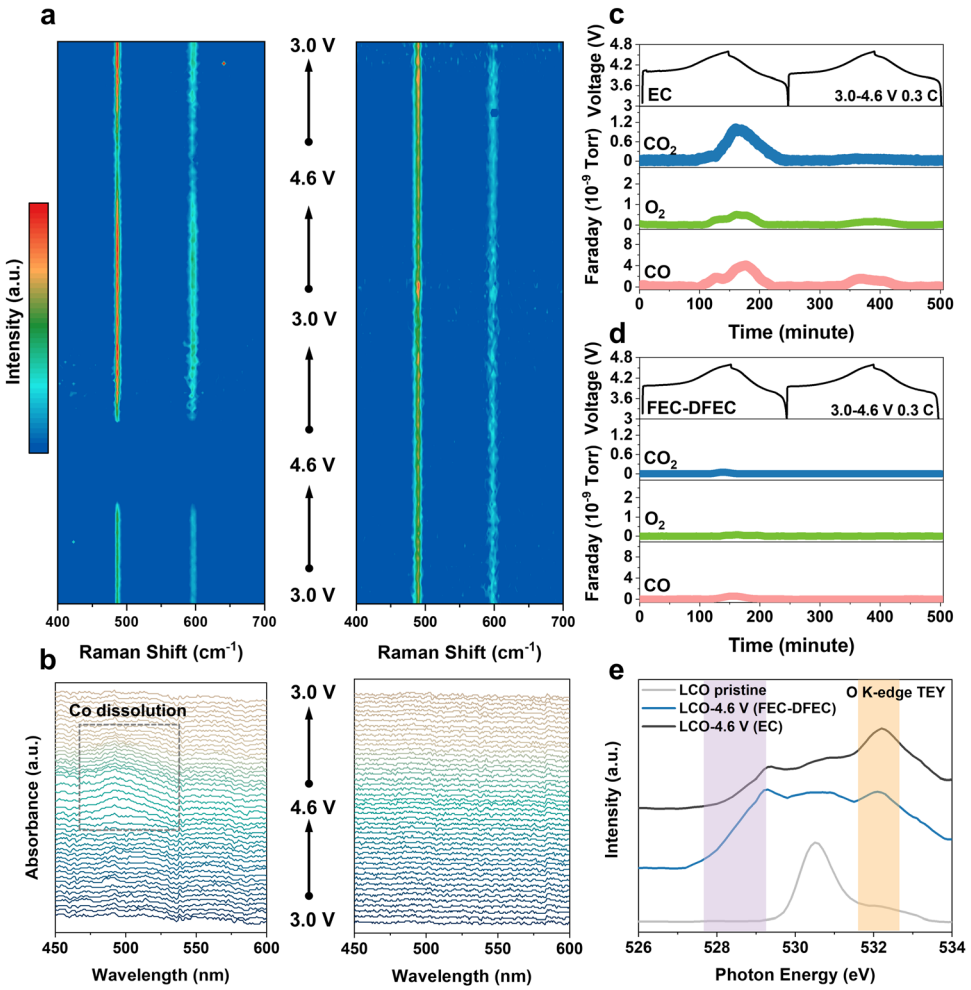


Fig. 3 Characterizations of the LCO/electrolyte interfacial side reaction. (a) *In situ* Raman spectra of the LCO||Li half cells in the EC and FEC–DFEC electrolytes in the voltage range of 3.0–4.6 V at a constant voltage scanning of 0.2 mV $s^{-1}$. (b) *In situ* UV-vis characterization in the voltage range of 3.0–4.6 V at a constant voltage scanning of 0.2 mV $s^{-1}$. The *in situ* DEMS tests of LCO||Li cells in (c) EC and (d) FEC–DFEC electrolytes in the voltage range of 3.0–4.6 V. (e) O K-edge spectra of TEY mode from sXAS measurements of pristine LCO and LCO with two types of electrolytes at 4.6 V after 10 cycles in the voltage range of 3.0–4.6 V.

The interfacial reaction can be further detected *via in situ* differential electrochemical mass spectrometry (DEMS) tests (Fig. 3(c) and (d)), in which the gas release from the LCO||Li cells is presented for the initial two cycles in the voltage range of 3.0–4.6 V. For the LCO||Li cell in the EC electrolyte, massive contents of $CO_2$, $O_2$ and CO are released in the high-potential range during the first cycle, which continuously proceeds in the second cycle. The obvious gas release is attributed to the following aspects: (i) the decomposition of EC and EMC solvents is aggravated by highly oxidative $Co^{4+}/O^{n-}$ ($0 < n < 2$), and (ii) HF constantly attacks the LCO surface upon charging, deteriorating the surface O loss. When compared, there is nearly no gas release observed in the FEC–DFEC electrolyte during the initial cycles, indicating the optimized interfacial reaction by effective electrolyte regulation. Furthermore, the soft X-ray absorption spectroscopy (sXAS) was applied to identify the reinforced structure stability by the solvent regulation. Fig. 3(e) compares the O K-edge spectra (TEY mode) results of pristine LCO and LCO at the charged state (at 4.6 V, after 10 cycles) in EC and FEC–DFEC electrolytes, respectively. For pristine LCO, the peak located at a photon energy of 530.5 eV corresponds to the hybridization of $Co^{3+}$ ($e^*_g$)–O 2p. For LCO charging to 4.6 V, the peaks located at photon energies of 529 eV and 527 eV emerge, corresponding to the hybridization of $Co^{4+}$ ($e^*_g$)–O 2p and $Co^{4+}$ ($t_{2g}$)– O 2p, indicating the much more remarkable ascending of Co valence in the surface for LCO in the FEC–DFEC electrolytes than in the EC electrolyte.[35] Meanwhile, the peaks located at ~532 eV also arise obviously, illustrating the formation of low-valence Co (such as $Co_3O_4$ or CoO) or $Li_2CO_3$ on the LCO surface, and the relative peak intensity is obviously higher for LCO at 4.6 V in the EC electrolyte than in the FEC–DFEC electrolyte.[36,37] We further conducted cryogenic transmission electron microscopy (cryo-TEM) measurements to characterize the surface region of LCO in different electrolytes after 10 cycles in the voltage range of 3.0–4.6 V. Fig. S22 (ESI†) indicates that the uneven surface

structure damage and CEI layer distribute on LCO, indicating that serious interfacial side reactions occur on LCO in the EC electrolyte, while LCO in the FEC–DFEC electrolyte exhibits intact particle and thin CEI layer with a thickness of less than 5 nm. In summary, the solvents' decomposition induced by oxidative $Co^{4+}/O^{n-}$ ($0 < n < 2$) and surface structure degradation of LCO with severe Co/O loss can be largely alleviated by using the FEC–DFEC electrolyte.

### Formation of robust CEI

As discussed above, the regulation of IHP and progressive construction of the CEI layer on the LCO surface in the FEC–DFEC electrolyte are responsible for the reduced interfacial side reactions, thus it is critical to dissect its structure and composition to understand the optimization mechanism. Herein, the structure electrochemistry in the LCO/electrolyte interface was first characterized by *in situ* EIS, as shown in Fig. S23a and b (ESI†). The EIS curves can be fitted and resolved to obtain two significant parameters (Fig. S23c and d, ESI†), *i.e.*, the surface film resistance ($R_{sf}$) referring to the property of CEI/SEI, and the charge transfer resistance ($R_{ct}$) referring to the property of the LCO surface after 10 cycles.[38] As observed, the FEC–DFEC electrolyte leads to more stable CEI/SEI formation due to the slight fluctuation of $R_{sf}$ values during the cycle, and better surface $Li^+$ transport kinetics with remarkably decreased $R_{ct}$ values. Fig. 4(a)–(d), Fig. S24 and S25 (ESI†) compare the cryo-TEM morphologies of LCO in different particles after 100 cycles in the EC and FEC–DFEC electrolytes, respectively. During the cycles, a loose and non-uniform CEI is formed on the LCO surface in the EC electrolyte (Fig. 4(a) and (b)), while a dense and homogeneous CEI with a thickness of 20 nm is formed in the FEC–DFEC electrolyte (Fig. 4(c) and (d)). In addition, as analyzed from the fast Fourier transform (FFT), the CEI formed in the EC electrolyte contains LiF and some amorphous species, while for the CEI formed in the FEC–DFEC electrolyte, there are large amounts of inorganic species including $Li_3PO_4$, LiF and $Li_2CO_3$.

The in depth X-ray photoelectron spectroscopy (XPS) was further applied to characterize the chemical compositions of CEI on LCO and correlated SEI on the Li anode after 100 cycles. In Fig. S26 (ESI†), the analyses of C 1s, O 1s, F 1s, P 2p, and Li 1s XPS results were performed, and the illustration of the fitted

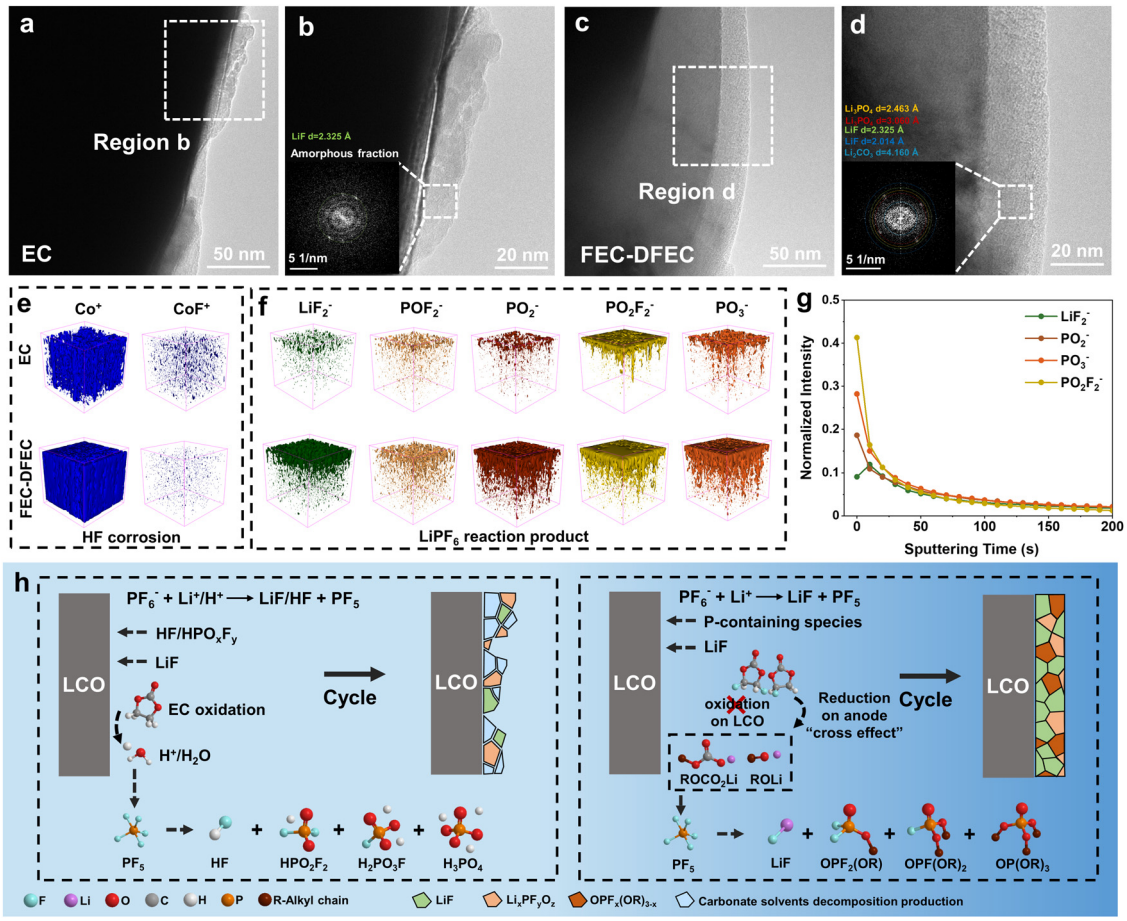


Fig. 4 Morphology and composition analyses of the LCO CEI layer. Cryo-TEM characterizations of the LCO CEI layer and FFT analysis after 100 cycles of LCO||Li cells in (a) and (b) EC and (c) and (d) FEC–DFEC electrolytes in the voltage range of 3.0–4.6 V at 1C. (e) and (f) The 3D reconstruction of diverse types of secondary-ion fragments for the LCO/electrolyte interface in the EC and FEC–DFEC electrolyte. (g) The distribution of $LiF_2^-$, $POF_2^-$, $PO_2^-$, $PO_3^-$, and $PO_2F_2^-$ species in the CEI layer from outside to inside. (h) Schematic of the LCO CEI formation during the cycle in EC and FEC–DFEC electrolytes.

 

results are clarified in detail in ESI.† Generally, in the EC electrolyte, the CEI on LCO surface contains the $PF_6^-$ decomposition-derived $LiF/Li_xPO_yF_z$ inorganics and solvent decomposition-derived organics, mainly due to the expense of forming more corrosive species (Fig. S26, ESI†). In addition, the SEI on Li metal has a similar composition accompanied by obvious Co deposition, as shown in Fig. S27 and S28 (ESI†). The characteristics of CEI/SEI in FEC–DFEC electrolyte based on XPS results can be illustrated as follows. First, there is no visible signal of Co detected on the surface of the cycled Li anode in the FEC–DFEC electrolyte, indicating the reduced formation of corrosive species and cross effect of Co during the cycles. Second, it shows a lower signal peak of Co–O lattice in the O 1s spectra, indicating the well-covered CEI to protect the LCO surface from corrosion. Third, there appears a new peak at 283.5 eV in the C 1s spectra, referring to the formation of organic species due to the ''cross effect'' of the decomposition of FEC/DFEC solvents from the anode side, which will be discussed subsequently.[39–42] Fourth, as more $PF_6^-$ ions are participating in the $Li^+$ solvation structure, there exist more LiF inorganics, while the content of P-containing species also increases with few Co dissolution (including $Li_xPO_yF_z$, $OPF_x(OR)_y$ and phosphate ($Li_3PO_4$, $OP(OR)_3$), in which R represents the alkyl chain), resulting in the uniform and robust CEI in the FEC–DFEC electrolyte.[43,44] Thus, based on the FEC–DFEC electrolyte, both the CEI on the LCO side and the SEI on the Li anode side are robust and uniform, which is vital for the enhanced cell performances under HV operation.

To further understand the mechanism of robust CEI formation, the spatial distribution of species in the CEI layers on the LCO surface was investigated by time-of-flight secondary ion mass spectrometry (TOF-SIMS) measurements. Fig. 4(e) shows a seriously corroded LCO surface with Co loss and generating Co–F species in the EC electrolyte, while in the FEC–DFEC electrolyte, the LCO surface is well maintained with nearly no visible signs of corrosion and Co–F species, which indicates the inhibition of corrosive species (such as HF and $HPO_xF_y$) in the FEC–DFEC electrolyte. However, Fig. 4(f) and Fig. S29 (ESI†) display the more uniform and robust spatial distributions of the $LiF_2^-$, $POF_2^-$, $PO_2^-$, $PO_2F_2^-$, and $PO_3^-$ species in the CEI formed in the FEC–DFEC electrolyte than that formed in the EC electrolyte. Combining the XPS results (Fig. S26, ESI†), it suggests that in the FEC/DFEC electrolyte, there are more $PF_6^-$ anions participating in the $Li^+$ solvation structure, leading to a different reaction pathway in comparison with the hydrolysis reaction in the EC electrolyte, thereby avoiding the formation of corrosive species but promoting the generation of P–O species. Fig. 4(g) shows the variations in the distribution of CEI products from surface to inside. It illustrates that $LiF_2^-$ seems to locate in the inner layer of CEI, while the $POF_2^-$, $PO_2^-$, $PO_2F_2^-$, and $PO_3^-$ species tend to locate in the outer layer of CEI. That is to say, upon cycles, the $PF_6^-$ anions enrich in the IHP region of the LCO/electrolyte interface and tend to preferentially deposit on the surface of LCO, forming the $PF_5$ and inner LiF species. Then, the $PF_5$ species further reacts with the reduction products of FEC/DFEC (*i.e.* lithium alkyl carbonates ($ROCO_2Li$) and lithium alkoxide (ROLi), as shown in Fig. S30, ESI†), forming more P-containing organic species in the outer layer (*i.e.*, $OPF_x(OR)_y$ and $OP(OR)_3$), corresponding to the P/F/O-containing species in the TOF-SIMS results.[41,45–48] Moreover, the $Li_xPO_yF_z/Li_3PO_4$ inorganics shown in XPS and cryo-TEM results are related to the further decomposition of $OPF_x(OR)_y$ and $OP(OR)_3$ species.

Furthermore, we assemble the LCO||$Li_4Ti_5O_{12}$ (LTO) full cells to confirm the ''cross effect'' of reduction products of FEC/DFEC from the Li/graphite anode (Fig. S31, ESI†). The XPS spectra of the LCO cathode electrode with different etching times after 50 cycles of LCO||LTO cells indicate that both the Li–O–C peak (located at 283.5 eV in the C 1s spectra) and the P–O peak (located at 134 eV in the P 2p spectra) are absent on the LCO surface (Fig. S32, ESI†). Besides, the cryo-TEM images and FFT results of different LCO particles (Fig. S33, ESI†) show that plenty of LiF nanoparticles deposit on the LCO surface, and the near-surface region of LCO still remains a pure layered phase. The enrichment of LiF component and the stable surface structure of LCO can be attributed to the $PF_6^-$ anions and anti-oxidative FEC/DFEC solvent-dominant interface chemistry in the IHP of LCO in the FEC–DFEC electrolyte, which is consistent with LCO cycled in LCO||Li cells. However, the lack of P–O XPS signal and $Li_3PO_4$ inorganic components can be attributed to the flat and high potential plateau of the LTO anode (at about 1.55 V *vs.* $Li^+/Li$), which inhibit the FEC/DFEC reduction on the anode side to some extent, and further affect the CEI evolution process. Additionally, the poor cycling stability of LCO||LTO cells may be attributed to the catalytic activity of the LTO surface, which can induce some interfacial side reactions accompanied by gas release.[49,50]

Combining the cryo-TEM, XPS, and TOF-SIMS results, the mechanism of forming a robust CEI on the LCO surface is fully illustrated in Fig. 4(h). In the EC electrolyte, during the cycles, the oxidation of EC solvents leads to the generation of $H_2O/H^+$ and promotes the hydrolysis of $PF_6^-$ anions to form some corrosive species (such as, HF and $HPO_xF_y$). These corrosive species not only cause surface structure degradation, but also obstruct the formation of a well-protective CEI on the LCO surface. As a result, a loose and non-uniform CEI is formed on the LCO surface. In contrast, in the FEC–DFEC electrolyte, during the cycles, the solvents are much stable to resist the oxidation on the LCO surface. Besides, in the IHP region of the LCO/electrolyte interface, the $PF_6^-$ anions are more concentrated due to the regulation of the solvation chemistry, which promotes more deposition of $LiF/Li_xPO_yF_z/Li_3PO_4$ inorganics and P-containing organics in the CEI, under the synergy of reduction products of FEC/DFEC. Consequently, the CEI formed in the FEC–DFEC electrolyte presents a chemo-mechanically stable feature, which can effectively reduce the $Co^{4+}/O^{n-}$ ($0 < n < 2$)-induced interfacial side reaction and the surface degradation of LCO, especially during long-term cycles.

### Long-term characterizations

As discussed above, a robust CEI with high chemo-mechanical stability and better $Li^+$ transport kinetics is achieved in the

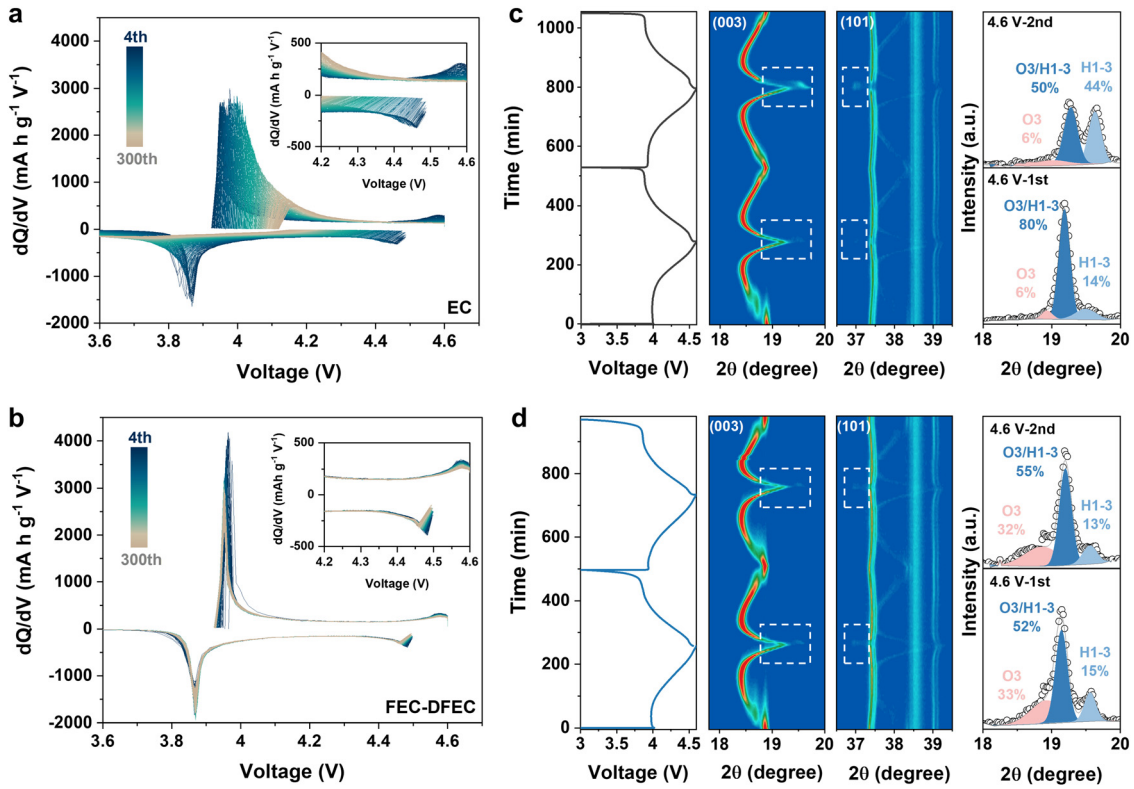


Fig. 5 Influence of electrolyte regulation on the phase transition of LCO. The d$Q$/d$V$ curves during the cycling of LCO||Li cells in (a) EC and (b) FEC–DFEC electrolytes in the voltage range of 3.0–4.6 V at 1C. The *in situ* XRD measurements and the (003) peak resolving of LCO at 4.6 V in (c) EC and (d) FEC–DFEC electrolytes in the voltage range of 3.0–4.6 V at 0.25C.

FEC–DFEC electrolyte, which enhances the reversibility of bulk phase transition in return and finally enables the long-term cycling stability of LCO. Here, the d$Q$/d$V$ curves and *in situ* XRD patterns were utilized to confirm this perspective. In Fig. 5(a) and (b), the redox peaks in the potential ranges of 3.9–4.0 V and 4.5–4.6 V in d$Q$/d$V$ curves represent the O3/O3′ and O3′/H1-3 phase transitions, respectively, in which, the latter peaks correlate with the sliding of the O–Co–O layer.[6,51] In the EC electrolyte, the phase transition reversibility of LCO is not satisfactory, *i.e.*, as the cycle proceeds, the potential difference between the oxidation and reduction peaks increases gradually for O3/O3′ phase transitions and vanishes for O3′/H1-3 phase transitions after 300 cycles. In contrast, LCO cycled in the FEC–DFEC electrolyte exhibits highly reversible phase transitions, showing stabilized $Li^+$ (de)intercalation from bulk LCO, which is due to the reduced surface degradation and the optimized CEI.

The *in situ* XRD patterns are employed to further probe the influence of electrolyte regulation on the phase transition of LCO (Fig. 5(c) and (d)). When charged to voltages beyond 4.5 V, LCO in the EC electrolyte shows a more obvious O3′/H1-3 phase transition than that in the FEC–DFEC electrolyte, as characterized by the peak separation of (003) and (101) peaks. Furthermore, when charged to 4.6 V, the (003) peaks of LCO can be divided into three peaks, *i.e.* O3′, O3′/H1-3 (a transition state from O3′ to H1-3) and H1-3.[35,52] For LCO in the FEC–DFEC electrolyte, qualitatively, the percentages of O3′, O3′/H1-3, and H1-3 are 33%, 52%, and 15% in the 1st cycle, and 32%, 55%, and 13% in the 2nd cycle, respectively. For LCO in the EC electrolyte, the percentages of O3′, O3′/H1-3, and H1-3 are 6%, 80%, and 14% in the 1st cycle, and 6%, 50%, and 44% in the 2nd cycle, respectively. The above-mentioned results indicate that, in the FEC/DFEC electrolyte, in a fully charged state, LCO contains more O3′ phases in the FEC–DFEC electrolyte, indicating the reduced slippage of O–Co–O layers. In addition, we consider that the origin of a higher degree of O3/H1-3 phase transition in the EC electrolyte during the initial two cycles is due to the formation of a thin surface spinel phase, with a thickness of about 2–5 nm (Fig. S34a and b, ESI†), which is attributed to the interfacial reactions between the LCO surface and the EC electrolyte in the 1st charging process. As a result, the polarization of the LCO electrode can be reduced to a certain extent, resulting in more $Li^+$ being extracted from LCO upon the activation process in the initial two cycles.[53] On the contrary, due to the regulated interface stability of LCO in the FEC–DFEC electrolyte, there is no activation process on the LCO surface, which remains as a layered structure at 4.6 V (Fig. S34c and d, ESI†). After 100 cycles, the layered structure of LCO is still well maintained in the FEC–DFEC electrolyte (Fig. S35, ESI†). Additionally, the worse cycle life of LCO in the EC electrolyte can hardly be related to the higher delithiation depth of LCO in the 1st and 2nd charging processes, but is

 

closely related to the severe surface structure deterioration due to the accumulated corrosive species in the LCO/electrolyte interface, and the formation of non-protective CEI in long-term cycles (Fig. 4 and Fig. S22, S26, ESI†).

To further probe the influence of solvents' regulation on the surface degradation of LCO during long-term cycles, the galvanostatic intermittent titration technique (GITT), EIS, SEM and TEM characterizations were performed. As observed in Fig. S36 (ESI†), according to the GITT curves, the calculated diffusion coefficient of $Li^+$ ($D_{Li^+}$) for LCO in the FEC–DFEC electrolyte after 100 cycles is significantly higher than that in the EC electrolyte. This reinforced and stabilized $D_{Li^+}$ value for LCO in the FEC–DFEC electrolyte is mainly attributed to the reduced surface degradation, thereby promoting faster $Li^+$ diffusion kinetics. Fig. S37a–c (ESI†) presents the EIS measurements of LCO after different cycles, and the fitted results of $R_{sf}$ and $R_{ct}$, in the EC and FEC–DFEC electrolytes.[54] Particularly, after 100 cycles, the $R_{ct}$ value for LCO in the FEC–DFEC electrolyte is only 300 Ω, far below that of 2300 Ω in the EC electrolyte, demonstrating a much better $Li^+$ transport kinetics across the stable surface structure. Then, the distribution of relaxation times (DRT) was further applied to analyze $R_{CEI}$ and $R_{SEI}$, which can decouple the intertwined electrochemical steps by capturing their time characteristics (Fig. S37d, ESI†). It is noted that $R_{SEI}$ and $R_{CEI}$ both show increased signal intensity and shift to larger relaxation time $\tau$ in the EC electrolyte, demonstrating the sluggish $Li^+$ transport through SEI and CEI due to severe interfacial side reactions, while for the FEC–DFEC electrolyte, the $R_{SEI}$ values hold steady and $R_{CEI}$ show decreased signal intensity and shift to a lower relaxation time $\tau$, which suggests a stable SEI layer and a progressively optimized CEI layer (Fig. 4(c)).[55,56]

The cyclic microstructural changes of LCO in different electrolytes were directly observed by SEM and cross-section TEM. As shown in Fig. S38 and S39 (ESI†), after the cycles, obvious cracks across the overall LCO particles can be observed in the EC electrolyte, while there is no visible crack observed in the FEC–DFEC electrolyte, which can be attributed to the following aspects: (i) the robust and uniform CEI on the LCO surface enables the steady $Li^+$ (de)intercalation from LCO bulk and (ii) the comprehensive result of surface structure stabilization and enhanced phase transition reversibility. In Fig. 6(a)

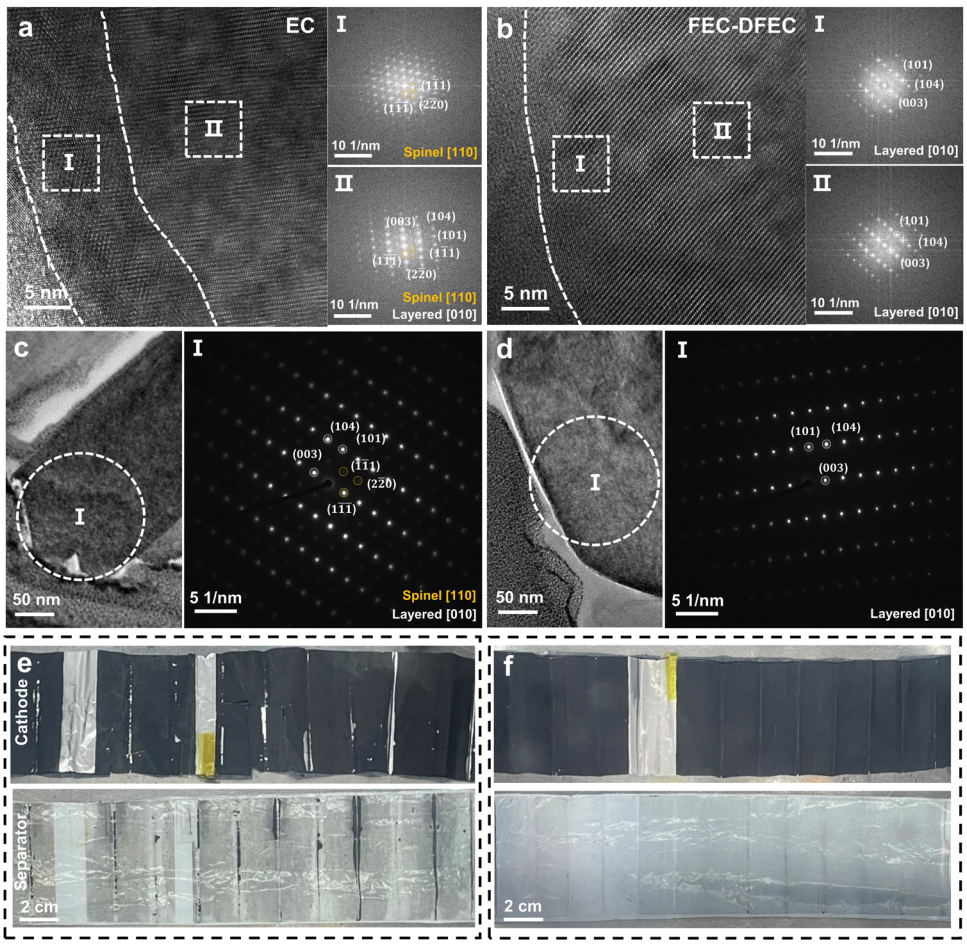


Fig. 6 Long-term characterizations. TEM and corresponding FFT results of LCO after 100 cycles of LCO||Li cells in (a) EC and (b) FEC–DFEC electrolytes in the voltage range of 3.0–4.6 V at 1C, and corresponding large-scale TEM and SAED results of LCO in (c) EC and (d) FEC–DFEC electrolytes. The digital photograph of the positive plate and separator of disassembled LCO||graphite pouch type full cells after 500 cycles in (e) EC and (f) FEC–DFEC electrolytes in the voltage range of 3.0–4.55 V at 1C.

and (b), the surface structure analyses *via* TEM and the correlated diffraction patterns were performed. As observed, the LCO surface cycled in the EC electrolyte shows an obvious spinel layer with a thickness of about 15 nm, and its subsurface region exhibits a hybrid of layered and spinel phases, indicating the serious irreversible phase transitions. In contrast, the FEC–DFEC electrolyte leads to the well-preserved layered structure of LCO in both the surface and subsurface regions, illustrating the stabilization of the LCO surface for better $Li^+$ diffusion with more reversible capacity delivery. As reported previously, the formation of thick surface spinel phase is mainly attributed to the O loss at HV, leading to high $R_{ct}$ of cycled LCO in the EC electrolyte. Besides, in Fig. 6(c) and (d), the selected area electron diffraction (SAED) patterns were applied to reveal the surface structure of LCO, in a more macroscopic field with a circular area of 150 nm in diameter. The results show an obvious spinel phase existing in the surface region of LCO in the EC electrolyte, while in the FEC–DFEC electrolyte, the LCO surface shows a pure layer phase structure.

As discussed above, the stabilization of LCO originated from the well-protective CEI layer with significantly reduced corrosive species. To confirm this inference, the LCO||graphite pouch cell after 500 cycles in the voltage range of 3.0–4.55 V was disassembled, and Fig. 6(e) and (f) show the digital photographs of the LCO electrodes and separators in two electrolytes. We observe that, in the EC electrolyte, the LCO electrode is severely damaged with the active slurry detaching from the Al foils, and the separator is also seriously contaminated by the Co dissolution and severe side reactions, due to the long-term corrosion from corrosive species. In contrast, in the FEC–DFEC electrolyte, the LCO electrode maintains its pristine state, and the separator is clean and smooth, indicating much lesser corrosive issues. Further XPS analyses were employed to characterize the LCO electrode and graphite anode of pouch cells, as shown in Fig. S40 and S41 (ESI†). In the EC electrolyte, $Li_xPO_yF_z$ species exist in the CEI of LCO due to the hydrolysis of $LiPF_6$, and more Co deposits exist on the graphite anode due to the Co dissolution from LCO. However, in the FEC–DFEC electrolyte, more LiF and P-containing species are observed at the interface of LCO, with no Co dissolution existing on the graphite anode, mainly due to the reduced corrosive species *via* solvent regulation.

Above all, the stabilization mechanism of LCO in the FEC–DFEC electrolyte is illustrated in Fig. 7. In the EC electrolyte, during the cycle, the dehydrogenation/oxidation of EC solvents at the LCO/electrolyte interface leads to the formation of $H_2O$/$H^+$, and subsequently, the hydrolysis of $PF_6^-$ produces massive amounts of corrosive species such as HF and $HPF_2O_2$. These corrosive species not only cause surface degradation *via* promoting Co/O loss from the LCO surface, but also obstruct the formation of a well protective CEI. After long-term cycles, LCO suffers from severe surface structure degradation, which seriously blocks the $Li^+$ ion transport across the LCO surface, thus leading to a rapid capacity decay. When compared, in the FEC–DFEC electrolyte, the interfacial side reaction induced by oxidative $Co^{4+}/O^{n-}$ and the generation of corrosive species are

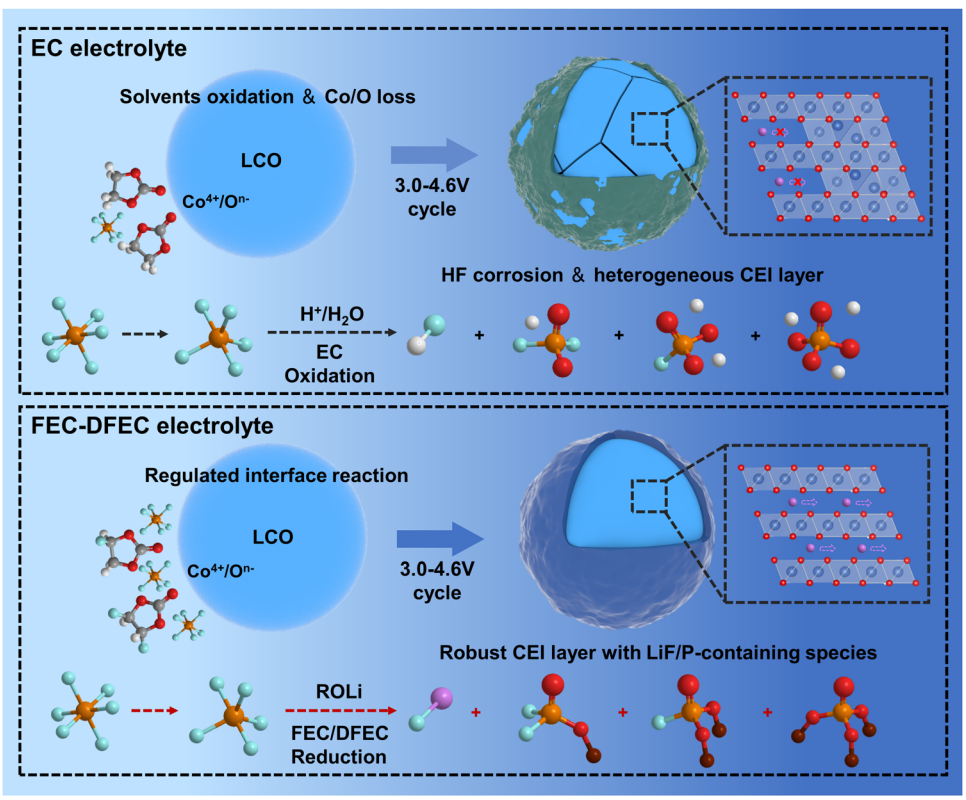


Fig. 7 Schematic of the mechanism of stabilizing $LiCoO_2$ at 4.6 V in the FEC–DFEC electrolyte.

 

greatly inhibited due to the solvents' regulation, in which the $PF_6^-$ anions enrich and react in the IHP region of the LCO/electrolyte interface and promote the formation of a uniform and robust CEI, which further protect the integrity of LCO with steady $Li^+$ transport kinetics, and ensure the reversibility of bulk phase transition. Consequently, LCO exhibits both enhanced cycling and rate performances in the designed FEC–DFEC electrolyte.

Furthermore, we summarize the synthesis technology of fluorine-containing carbonates (Table S3, ESI†) and the recycle technology of the used electrolyte (Table S4, ESI†), to discuss the feasibility of widespread applications of such electrolytes with high-concentration fluorinated solvents.[57,58] We believe that, with the development of advanced synthesis methods of FEC/DFEC, *i.e.* development of high-performance, low-cost catalysts, and advanced purification technology of the halogen exchange reaction method, or the industrialization of the electrochemical fluorination method, combined with the maturity of the electrolyte recycling technology, the price of fluorine-containing carbonates will continue to decrease (Fig. S42, ESI†).[59–61] Additionally, the demand for high-voltage and high-performance electrolytes in the market will continue to grow in the future, which will inevitably push more capital, talent, and resources to gather in the links of research, production, and recycling of high-voltage electrolytes. Thus, we expect that it is possible to use fluorinated solvent electrolytes in a large-scale, low-cost and environment-friendly way.

## Conclusions

In summary, this work provided a new insight to understand the optimization effect of solvent regulation. In traditional EC electrolytes, the structural degradation of LCO during the cycle at 4.6 V (*vs.* $Li/Li^+$) mainly originated from the severe surface Co/O loss induced by corrosive species. Replacing the unstable EC solvent with the FEC/DFEC solvents can effectively regulate the $Li^+$ solvation structures, comprising anti-oxidative fluorinated solvents and highly coordinated $PF_6^-$ anions. This optimized electrolyte solvation structure leads to modified interface chemistry of $PF_6^-$ anions, constructing a robust and uniform CEI and reducing the generation of corrosive species, ensuring the well-maintained layered structure of LCO and reversibility of bulk phase transition during long-term cycles. As a result, the LCO cathode shows significantly enhanced rate capability and long-term cycling stability at a high cut-off voltage of 4.6 V, with a high capacity retention of 85.5% after 1000 cycles in LCO||Li cells and 85.7% after 500 cycles in LCO||graphite pouch cells.

## Author contributions

F. P., Q. Z. M. L. and G. Z. proposed and designed the project. H. R. performed electrochemical measurements and carried out characterizations. H. R. and Y. L. conducted and processed TOF-SIMS and XPS measurements. H. R. and S. C. conducted and processed Raman and UV measurements. H. R., H. Y. and J. F. performed the fabrication and performance testing of the pouch cells. H. R. and X. W. conducted the *in situ* XRD measurements. M. Z. conducted the theoretical calculation. H. R., W. H. and W. Z. conducted and processed the TEM measurements. G. Z., T. L. and L. Y. commented on electrolyte formulations. All authors discussed the results and revised or commented on the manuscript.

## Data availability

The data supporting the findings of this study are included within the main article and ESI.†

## Conflicts of interest

The authors declare no competing interests.

## Acknowledgements

This work is financially supported by the National Natural Science Foundation of China (52102201), the Basic and Applied Basic Research Foundation of Guangdong Province (2021B1515130002), and Soft Science Research Project of Guangdong Province (2017B030301013). This work also gratefully acknowledges support from the U. S. Department of Energy (DOE), Office of Energy Efficiency and Renewable Energy, Vehicle Technologies Office.

## Notes and references

1 M. Cai, Y. Dong, M. Xie, W. Dong, C. Dong, P. Dai, H. Zhang, X. Wang, X. Sun, S. Zhang, M. Yoon, H. Xu, Y. Ge, J. Li and F. Huang, *Nat. Energy*, 2023, **8**, 159–168.
2 Y. Zhang, Y. Katayama, R. Tatara, L. Giordano, Y. Yu, D. Fraggedakis, J. G. Sun, F. Maglia, R. Jung, M. Z. Bazant and Y. Shao-Horn, *Energy Environ. Sci.*, 2020, **13**, 183–199.
3 C. Lin, J. Li, Z. W. Yin, W. Huang, Q. Zhao, Q. Weng, Q. Liu, J. Sun, G. Chen and F. Pan, *Adv. Mater.*, 2023, **36**, 2307404.
4 J. Zhang, P. F. Wang, P. Bai, H. Wan, S. Liu, S. Hou, X. Pu, J. Xia, W. Zhang, Z. Wang, B. Nan, X. Zhang, J. Xu and C. Wang, *Adv. Mater.*, 2022, **34**, 2108353.
5 X. Wang, H. Ren, Y. Du, Z. Li, W. Zhao, H. Ji, H. Yi, Q. Pan, J. Liu, Z. Lou, L. Zhou, F. Pan and Q. Zhao, *Nano Energy*, 2024, **125**, 109537.
6 H. Ren, W. Zhao, H. Yi, Z. Chen, H. Ji, Q. Jun, W. Ding, Z. Li, M. Shang, J. Fang, K. Li, M. Zhang, S. Li, Q. Zhao and F. Pan, *Adv. Funct. Mater.*, 2023, **33**, 2302622.
7 A. Yano, M. Shikano, A. Ueda, H. Sakaebe and Z. Ogumi, *J. Electrochem. Soc.*, 2016, **164**, A6116–A6122.
8 W. Ding, H. Ren, Z. Li, M. Shang, Y. Song, W. Zhao, L. Chang, T. Pang, S. Xu, H. Yi, L. Zhou, H. Lin, Q. Zhao and F. Pan, *Adv. Energy Mater.*, 2024, **14**, 2303926.

9 K. Kim, D. Hwang, S. Kim, S. O. Park, H. Cha, Y. S. Lee, J. Cho, S. K. Kwak and N. S. Choi, *Adv. Energy Mater.*, 2020, **10**, 2000012.
10 B. L. D. Rinkel, D. S. Hall, I. Temprano and C. P. Grey, *J. Appl. Chem. Sci.*, 2020, **142**, 15058–15074.
11 Y. Yan, S. Weng, A. Fu, H. Zhang, J. Chen, Q. Zheng, B. Zhang, S. Zhou, H. Yan, C.-W. Wang, Y. Tang, H. Luo, B.-W. Mao, J. Zheng, X. Wang, Y. Qiao, Y. Yang and S.-G. Sun, *ACS Energy Lett.*, 2022, **7**, 2677–2684.
12 C. L. Campion, W. T. Li and B. L. Lucht, *J. Electrochem. Soc.*, 2005, **152**, A2327–A2334.
13 G. G. Amatucci, J. M. Tarascon and L. C. Klein, *Solid State Ionics*, 1996, **83**, 167–173.
14 M. He, C.-C. Su, C. Peebles and Z. Zhang, *J. Electrochem. Soc.*, 2021, **168**, 010505.
15 C.-C. Su, M. He, M. Cai, J. Shi, R. Amine, N. D. Rago, J. Guo, T. Rojas, A. T. Ngo and K. Amine, *Nano Energy*, 2022, **92**, 106720.
16 E. Markevich, G. Salitra and D. Aurbach, *ACS Energy Lett.*, 2017, **2**, 1337–1345.
17 T. Fan, W. Kai, V. K. Harika, C. Liu, A. Nimkar, N. Leifer, S. Maiti, J. Grinblat, M. N. Tsubery, X. Liu, M. Wang, L. Xu, Y. Lu, Y. Min, N. Shpigel and D. Aurbach, *Adv. Funct. Mater.*, 2022, **32**, 2204972.
18 Z. Wang, Z. Sun, Y. Shi, F. Qi, X. Gao, H. Yang, H. M. Cheng and F. Li, *Adv. Energy Mater.*, 2021, **11**, 2100935.
19 A. Zhang, Z. Bi, G. Wang, S. Liao, P. Das, H. Lin, M. Li, Y. Yu, X. Feng, X. Bao and Z.-S. Wu, *Energy Environ. Sci.*, 2024, **17**, 3021–3031.
20 D. Aurbach, E. Markevich and G. Salitra, *J. Appl. Chem. Sci.*, 2021, **143**, 21161–21176.
21 N. Xu, J. Shi, G. Liu, X. Yang, J. Zheng, Z. Zhang and Y. Yang, *J. Power Sources Adv.*, 2021, **7**, 100043.
22 C.-C. Su, M. He, R. Amine, Z. Chen, R. Sahore, N. Dietz Rago and K. Amine, *Energy Storage Mater.*, 2019, **17**, 284–292.
23 Y. Yang, J. Wang, Z. Li, Z. Yang, B. Wang and H. Zhao, *ACS Nano*, 2024, **18**, 7666–7676.
24 J. Hu, W. Ren, X. Chen, Y. Li, W. Huang, K. Yang, L. Yang, Y. Lin, J. Zheng and F. Pan, *Nano Energy*, 2020, **74**, 104864.
25 C. Yan, H.-R. Li, X. Chen, X.-Q. Zhang, X.-B. Cheng, R. Xu, J.-Q. Huang and Q. Zhang, *J. Appl. Chem. Sci.*, 2019, **141**, 9422–9429.
26 X. Bogle, R. Vazquez, S. Greenbaum, A. van Wald Cresce and K. Xu, *J. Phys. Chem. Lett.*, 2013, **4**, 1664–1668.
27 Z. Yu, H. Wang, X. Kong, W. Huang, Y. Tsao, D. G. Mackanic, K. Wang, X. Wang, W. Huang, S. Choudhury, Y. Zheng, C. V. Amanchukwu, S. T. Hung, Y. Ma, E. G. Lomeli, J. Qin, Y. Cui and Z. Bao, *Nat. Energy*, 2020, **5**, 526–533.
28 R. Xu, C. Yan, Y. Xiao, M. Zhao, H. Yuan and J.-Q. Huang, *Energy Storage Mater.*, 2020, **28**, 401–406.
29 J. Zheng, J. Lu, K. Amine and F. Pan, *Nano Energy*, 2017, **33**, 497–507.
30 H. Zhang, Y. Huang, Y. Wang, L. Wang, Z. Song, H. Wang, C. Xu, X. Tian, S. Wang, J. Fang, W. Zhao, H. Cao, X. Yao, J. Yang, R. Tan, L. Yang, F. Pan and Y. Zhao, *Energy Storage Mater.*, 2023, **62**, 102951.
31 W. Dong, B. Ye, M. Cai, Y. Bai, M. Xie, X. Sun, Z. Lv and F. Huang, *ACS Energy Lett.*, 2023, **8**, 881–888.
32 W. Kong, J. Zhang, D. Wong, W. Yang, J. Yang, C. Schulze and X. Liu, *Angew. Chem., Int. Ed.*, 2021, **60**, 27102–27112.
33 S. Chen, G. Zheng, X. Yao, J. Xiao, W. Zhao, K. Li, J. Fang, Z. Jiang, Y. Huang, Y. Ji, K. Yang, Z.-W. Yin, M. Zhang, F. Pan and L. Yang, *ACS Nano*, 2024, **18**, 6600–6611.
34 M. Malik, K. H. Chan and G. Azimi, *RSC Adv.*, 2021, **11**, 28014–28028.
35 Z. Wu, G. Zeng, J. Yin, C.-L. Chiang, Q. Zhang, B. Zhang, J. Chen, Y. Yan, Y. Tang, H. Zhang, S. Zhou, Q. Wang, X. Kuai, Y.-G. Lin, L. Gu, Y. Qiao and S.-G. Sun, *ACS Energy Lett.*, 2023, **8**, 4806–4817.
36 C. Yogi, D. Takamatsu, K. Yamanaka, H. Arai, Y. Uchimoto, K. Kojima, I. Watanabe, T. Ohta and Z. Ogumi, *J. Power Sources*, 2014, **248**, 994–999.
37 J. Kikkawa, S. Terada, A. Gunji, T. Nagai, K. Kurashima and K. Kimoto, *J. Phys. Chem. C*, 2015, **119**, 15823–15830.
38 A. Yano, N. Taguchi, H. Kanzaki, M. Shikano and H. Sakaebe, *J. Electrochem. Soc.*, 2021, **168**, 050517.
39 A. Nimkar, N. Shpigel, F. Malchik, S. Bublil, T. Fan, T. R. Penki, M. N. Tsubery and D. Aurbach, *ACS Appl. Mater. Interfaces*, 2021, **13**, 46478–46487.
40 W. Zhang, S. Zhang, L. Fan, L. Gao, X. Kong, S. Li, J. Li, X. Hong and Y. Lu, *ACS Energy Lett.*, 2019, **4**, 644–650.
41 L. Gireaud, S. Grugeon, S. Laruelle, S. Pilard and J. M. Tarascon, *J. Electrochem. Soc.*, 2005, **152**, A850–A857.
42 J. Langdon and A. Manthiram, *Adv. Funct. Mater.*, 2021, **31**, 2010267.
43 Y.-C. Lu, A. N. Mansour, N. Yabuuchi and Y. Shao-Horn, *Chem. Mater.*, 2009, **21**, 4408–4424.
44 S. Tan, Z. Shadike, J. Li, X. Wang, Y. Yang, R. Lin, A. Cresce, J. Hu, A. Hunt, I. Waluyo, L. Ma, F. Monaco, P. Cloetens, J. Xiao, Y. Liu, X.-Q. Yang, K. Xu and E. Hu, *Nat. Energy*, 2022, **7**, 484–494.
45 Y. Zhang, D. Krishnamurthy and V. Viswanathan, *J. Electrochem. Soc.*, 2020, **167**, 070554.
46 B. Ravdel, K. M. Abraham, R. Gitzendanner, J. DiCarlo, B. Lucht and C. Campion, *J. Power Sources*, 2003, **119–121**, 805–810.
47 C. L. Campion, W. T. Li, W. B. Euler, B. L. Lucht, B. Ravdel, J. F. DiCarlo, R. Gitzendanner and K. M. Abraham, *Electrochem. Solid State Lett.*, 2004, **7**, A194–A197.
48 K. Kim, I. Park, S.-Y. Ha, Y. Kim, M.-H. Woo, M.-H. Jeong, W. C. Shin, M. Ue, S. Y. Hong and N.-S. Choi, *Electrochim. Acta*, 2017, **225**, 358–368.
49 J. Liu, P. Bian, J. Li, W. Ji, H. Hao and A. Yu, *J. Power Sources*, 2015, **286**, 380–387.
50 C. Han, Y.-B. He, M. Liu, B. Li, Q.-H. Yang, C.-P. Wong and F. Kang, *J. Mater. Chem. A*, 2017, **5**, 6368–6381.

 

51 A. Van der Ven, M. K. Aydinol and G. Ceder, *J. Electrochem. Soc.*, 1998, **145**, 2149–2155.
52 M. Hirooka, T. Sekiya, Y. Omomo, M. Yamada, H. Katayama, T. Okumura, Y. Yamada and K. Ariyoshi, *J. Power Sources*, 2020, **463**, 228127.
53 J.-H. Shim, K.-S. Lee, A. Missyul, J. Lee, B. Linn, E. C. Lee and S. Lee, *Chem. Mater.*, 2015, **27**, 3273–3279.
54 B. Zhang, L. Wang, Y. Zhang, X. Wang, Y. Qiao and S.-G. Sun, *J. Chem. Phys.*, 2023, **158**, 054202.
55 Y. Lu, C.-Z. Zhao, J.-Q. Huang and Q. Zhang, *Joule*, 2022, **6**, 1172–1198.
56 T. H. Wan, M. Saccoccio, C. Chen and F. Ciucci, *Electrochim. Acta*, 2015, **184**, 483–499.
57 A. Rensmo, E. K. Savvidou, I. T. Cousins, X. Hu, S. Schellenberger and J. P. Benskin, *Environ. Sci.: Processes Impacts*, 2023, **25**, 1015–1030.
58 Y. Wang, Z. Li, Y. Hou, Z. Hao, Q. Zhang, Y. Ni, Y. Lu, Z. Yan, K. Zhang, Q. Zhao, F. Li and J. Chen, *Chem. Soc. Rev.*, 2023, **52**, 2713–2763.
59 G. Ma, L. Wang, J. Zhang, H. Chen, X. He and Y. Ding, *Prog. Chem.*, 2016, **28**, 1299–1312.
60 E. Fan, L. Li, Z. Wang, J. Lin, Y. Huang, Y. Yao, R. Chen and F. Wu, *Chem. Rev.*, 2020, **120**, 7020–7063.
61 F. Arshad, L. Li, K. Amin, E. Fan, N. Manurkar, A. Ahmad, J. Yang, F. Wu and R. Chen, *ACS Sustainable Chem. Eng.*, 2020, **8**, 13527–13554.